Catalysis Science & Technology

ROYAL SOCIETY
OF **CHEMISTRY**
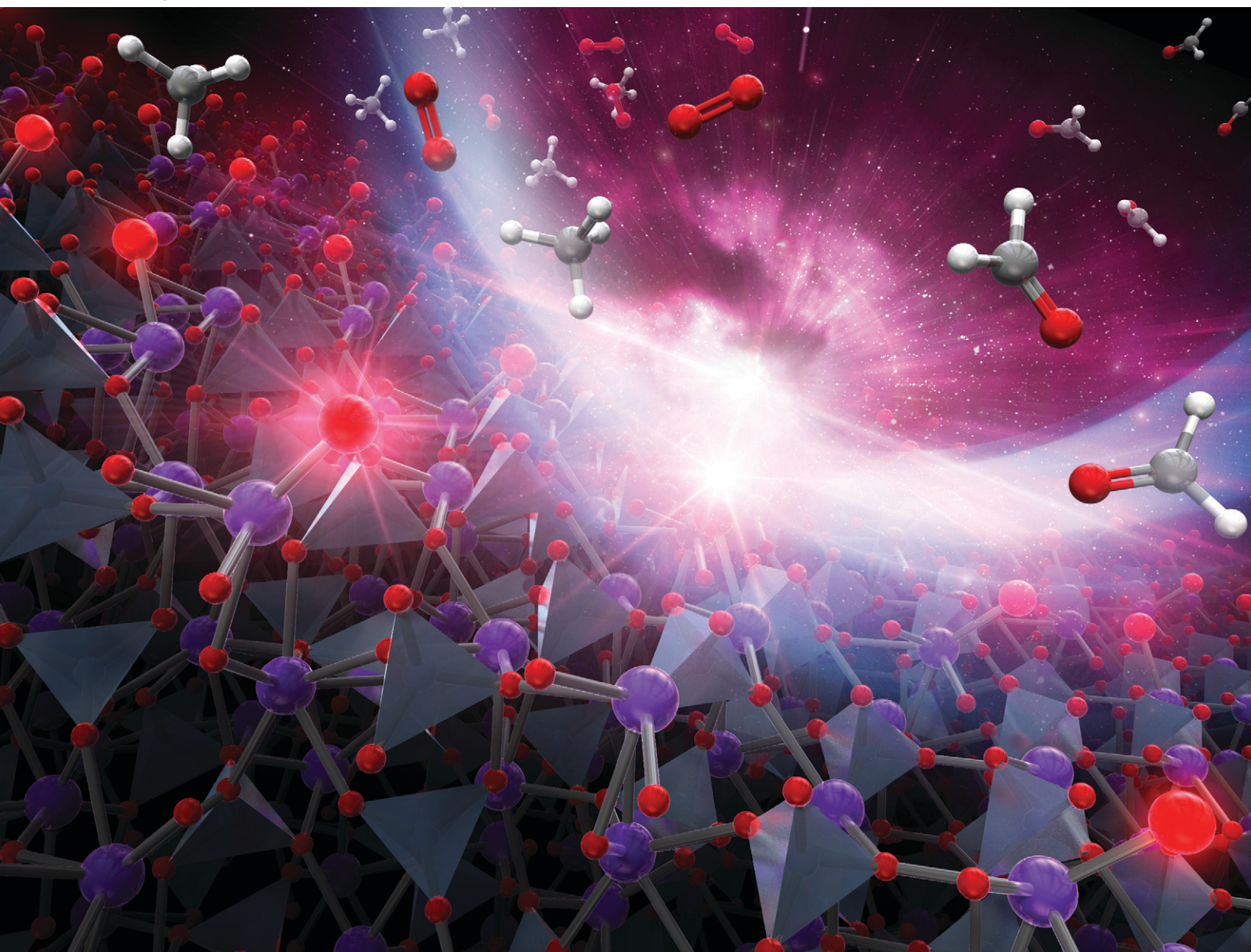
PAPER
Keigo Kamata *et al.*
Bismuth phosphate nanoparticle catalyst for direct oxidation
of methane into formaldehyde

PAPER

Check for updates

Bismuth phosphate nanoparticle catalyst for direct oxidation of methane into formaldehyde†

Aoi Matsuda,[a] Kazuhiko Obara,[a] Atsushi Ishikawa, [iD][b] Meng-Hsuan Tsai,[c] Chia-Hsin Wang,[c] Yu-Chuan Lin, [iD][d] Michikazu Hara [iD][a] and Keigo Kamata [iD] *[a]

The direct oxidation of methane (CH_4) to formaldehyde (HCHO) with molecular oxygen (O_2) as the sole oxidant was studied over various bismuth-based catalysts ($BiPO_4$, α-Bi_2O_3, β-Bi_2O_3) using a fixed-bed flow reactor. The catalytic activity of monoclinic $BiPO_4$ nanoparticles ($BiPO_4$-DEG) synthesized in a mixed solvent of diethylene glycol (DEG) and water for the direct oxidation of CH_4 was the highest among the catalysts tested. In high temperature region, $BiPO_4$-DEG was more selective for HCHO formation than $FePO_4$ nanoparticles. Based on mechanistic studies including the catalyst effect, kinetics, pulse-reaction experiments, infrared (IR) spectroscopy, *operando* near ambient pressure X-ray photoelectron spectroscopy (NAP-XPS), and density functional theory (DFT) calculations, surface active oxygen species generated on $BiPO_4$ possibly react with CH_4 to give HCHO as the primary product. In contrast, the phosphate units of $FePO_4$ nanoparticles react with CH_4 followed by rapid reoxidation to $FePO_4$.

1. Introduction

Methane (CH_4) has attracted attention as an important raw material due to its abundance around the world as a main component of natural gas and a low emitter of greenhouse gases such as carbon dioxide (CO_2) compared to coal and oil.[1] However, CH_4 is mainly used as an energy source for heating, cooking, and power generation. The use of CH_4 as a chemical feedstock is very small due to the difficulty in activating the strong C–H bond (440 kJ mol^{-1}).[2] Current CH_4 conversion into commodity chemicals and fuels is limited to indirect pathways *via* synthesis gas (CO + H_2) produced by energy- and capital-intensive reforming processes.[3] Therefore, the development of catalytic processes that can directly convert CH_4 into useful chemicals and fuels is an important and challenging subjects, and various effective thermocatalytic,[2,4–8] electrocatalytic,[9] and plasma- or electric-field assisted systems[10] have been reported for oxidative CH_4 upgrading and non-oxidative dehydrogenative aromatization.[11,12]

Various effective solid materials based on metal-exchanged zeolites,[14–18] metal oxides,[19–22] supported catalysts,[23–25] metal phosphates,[26–36] and metal organic frameworks[37,38] can function as efficient catalysts for oxidative upgrading of CH_4 such as oxidative coupling to ethylene (C_2H_4), oxygenation to methanol (CH_3OH) and/or formaldehyde (HCHO), and oxidative halogenation using O_2, H_2O_2, and N_2O as oxidants. In particular, V- and Mo-based catalysts and B_2O_3/Al_2O_3 are efficient catalysts for the oxidation of CH_4 into HCHO which is an important raw material as resins and polyfunctional alcohols.[39–42] The performance of V- and Mo-based catalysts is improved by the metal loading amounts and space velocity, and Cu–MoO_x catalysts selectively give HCHO in 1.0% yield (62% select.) for the CH_4 oxidation at 700 °C in the presence of water vapor.[41] Non-metallic B_2O_3-based catalysts exhibit high HCHO yield and selectivity, and molecular O_2 bonded to tri-coordinated BO_3 centers on B_2O_3 surfaces has been proposed as an active oxidant for CH_4 activation.[42]

Among the solid catalyst materials, we have also focused on metal phosphates with unique surface redox and acid–base properties for the direct oxidation of CH_4 with O_2 as the sole oxidant.[28,43,44] Monoclinic cerium orthophosphate ($CePO_4$) nanorods efficiently catalyze the oxidative coupling of CH_4 in an electric field without the need for external heating.[28,43] Trigonal iron phosphate ($FePO_4$) nanoparticles exhibits high activity for the selective oxidation of CH_4 into HCHO. The weakly-basic phosphate units likely contribute to

[a] Laboratory for Materials and Structures, Institute of Innovative Research, Tokyo Institute of Technology, 4259 Nagatsuta-cho, Midori-ku, Yokohama, Kanagawa 226-8503, Japan. E-mail: kamata.k.ac@m.titech.ac.jp

[b] Department of Transdisciplinary Science and Engineering, School of Environment and Society, Tokyo Institute of Technology, 2-12-1 Ookayama, Meguro-ku, Tokyo 152-8550, Japan

[c] National Synchrotron Radiation Research Center, 101 Hsin-Ann Rd., 30076, Hsinchu, Taiwan

[d] Department of Chemical Engineering, National Cheng Kung University, 1 University Rd., Tainan, 70101, Taiwan

† Electronic supplementary information (ESI) available. See DOI: https://doi.org/10.1039/d3cy00590a

5180 | *Catal. Sci. Technol.*, 2023, **13**, 5180–5189

This journal is © The Royal Society of Chemistry 2023

the suppression of complete oxidation to CO_2.[44] While the redox-active Lewis acidic metal sites of metal phosphates play an important role in the activation of CH_4 and O_2, the effect of metals and the reaction mechanism on the direct oxidation of CH_4 is still unclear. Herein, we focus on bismuth, which is used as the main catalyst component in industrial propylene oxidation processes.[45] Although bismuth phosphates (Fig. 1) have been mostly investigated for photocatalytic reactions,[46–51] their application to other reactions (*e.g.*, oxidative dehydrogenation,[52–54] ammoxidation,[55] decomposition,[56] isomerization,[57] aldol condensation[58]) including the direct oxidation of CH_4 has not been sufficiently explored.[23,26]

In this paper, we report the selective oxidation of CH_4 to HCHO with molecular oxygen (O_2) as the sole oxidant over a $BiPO_4$ catalyst using a fixed-bed flow reactor. $BiPO_4$ nanoparticles ($BiPO_4$-DEG) synthesized in a mixed solvent in DEG/water exhibit higher catalytic activity and selectivity for HCHO than other bismuth-containing catalysts (Fig. 1) and $FePO_4$ nanoparticles.[44] The mechanistic studies including the catalyst effect, pulse experiments, kinetics, operando analysis and density functional theory (DFT) calculations indicate that surface oxygen species generated on $BiPO_4$ possibly react with CH_4 to give HCHO as a primary product.

2. Experimental section

2.1. Instruments

X-ray diffraction (XRD), energy dispersive X-ray fluorescence spectroscopy (ED-XRF), Fourier transform infrared spectroscopy (FT-IR), thermogravimetry-differential thermal analysis (TG-DTA), H_2 temperature-programmed reduction (H_2-TPR), nitrogen adsorption–desorption, scanning electron microscopy (SEM), transmission electron microscopy (TEM), and X-ray photoelectron spectroscopy (XPS) were performed using previously described instruments.[44,59–61] The details are described in the ESI.†
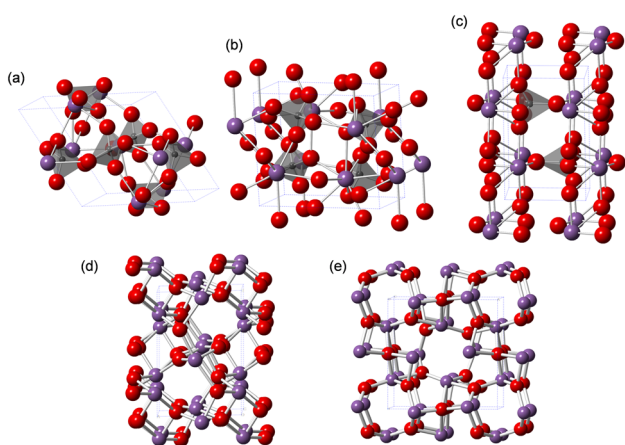

Fig. 1 Structures of (a) trigonal $BiPO_4 \cdot (H_2O)_{0.67}$, (b) monoclinic $BiPO_4$ ($P2_1/n$), and (c) monoclinic $BiPO_4$ ($P2_1/m$), (d) monoclinic α-Bi_2O_3, and (e) tetragonal β-Bi_2O_3. Purple, gray, and red spheres represent Bi, P, and O atoms, respectively.

2.2. Synthesis of $BiPO_4$-DEG

$NH_4H_2PO_4$ (1.035 g, 9 mmol) was dissolved in a mixed solution of diethylene glycol (DEG)/water (75 mL, 1/1 v/v). A DEG solution (30 mL) containing $Bi(NO_3)_3 \cdot 5H_2O$ (4.37 g, 9 mmol) was added dropwise into this phosphate solution followed by stirring for 60 min at room temperature. The resulting precipitates were collected by centrifugation, washed with ethanol (40 mL × 3), and dried at 110 °C overnight to obtain $BiPO_4 \cdot (H_2O)_{0.67}$ as a precursor. This precursor was calcined at 600 °C for 5 h to give $BiPO_4$-DEG (2.54 g, 93% yield).

2.3. Synthesis of $BiPO_4$-HT

$BiPO_4$-HT was synthesized by a hydrothermal (HT) reaction. $Bi(NO_3)_3 \cdot 5H_2O$ (6.00 mmol, 2.91 g) and $(NH_4)_2HPO_4$ (6.00 mmol, 0.792 g) were added to water (70 mL) and stirred for 30 min at room temperature. The resulting solution was transferred into a stainless steel autoclave with a Teflon vessel liner (TAF-SR type, Taiatsu Techno Corporation). After the solution was heated at 180 °C for 18 h, the precipitates were collected by filtration and washed with water (200 mL). The resulting precipitates were calcined at 600 °C for 5 h and the $BiPO_4$-HT catalyst was obtained (1.75 g, 96% yield).

2.4. Catalytic oxidation of CH_4 with O_2

The oxidation of CH_4 with O_2 over various bismuth-based catalysts was conducted in a fixed-bed continuous-flow reactor operated at atmospheric pressure. All of the catalysts were pressed into pellets, crushed, and sieved to 32–42 meshes before the reaction. The catalyst (100 mg) was loaded into a quartz reactor (2 mm inner diameter at the catalyst bed portion) over a plug of quartz wool. When using a quartz reactor with larger inner diameter (4 mm) under the conditions in Fig. 3(d), the HCHO yield was not changed but the CO yield increased, which likely indicates quenching effect. A reaction gas containing $CH_4/O_2/N_2$ in a molar ratio of 20/20/60 was used and the total gas flow rate was 10 sccm (*i.e.*, $CH_4/O_2/N_2$ = 2/2/6 sccm). After introduction of the reaction gas flow to the reactor, the reaction temperature was increased from room temperature to 600 °C at a heating rate of *ca.* 40 °C min⁻¹ and then held for 60 min. After the first sampling of the reaction gas, the temperature was decreased by 10 °C to 470 °C (420 °C in the case of $FePO_4$) every 60 min with periodic analysis of the reaction gas. The products (CO, CO_2, CH_3OH, HCHO, CH_3OCH_3, C_2H_6, C_2H_4) were analyzed using on-line gas chromatography (Shimadzu GC-8A) with a thermal conductivity detector (TCD) and two packed columns (a mixed column of Porapak-QS/-N and molecular sieves 5A). All of the lines and valves between the reactor exit and the gas chromatograph were heated to 120–130 °C to prevent condensation of the products. Details of the calculations of CH_4 conversion, yield, and selectivity are as follows: CH_4 conversion (%) = carbon of (CO, CO_2, HCHO)/carbon of input CH_4 × 100. Yield (%) = carbon of product/carbon of input CH_4 × 100. Selectivity (%) = yield/CH_4 conversion × 100.

This journal is © The Royal Society of Chemistry 2023

Catal. Sci. Technol., 2023, **13**, 5180–5189 | **5181**
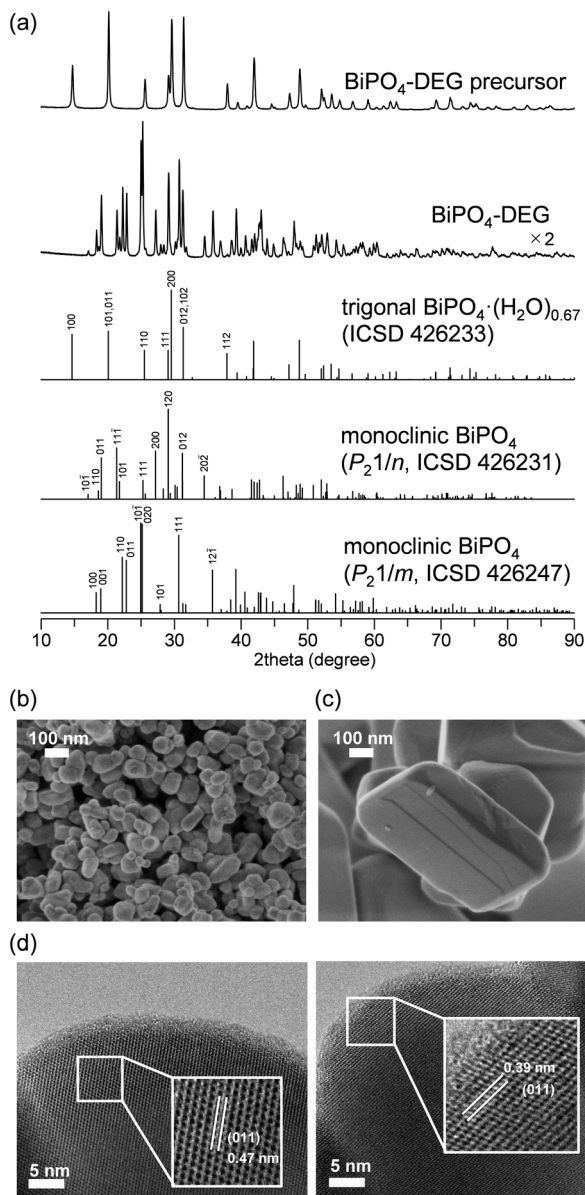
Fig. 2 (a) XRD patterns for $BiPO_4$-DEG precursor, $BiPO_4$-DEG, trigonal $BiPO_4 \cdot (H_2O)_{0.67}$ (ICSD 426233), monoclinic $BiPO_4$ (P_21/n, ICSD 426231), and monoclinic $BiPO_4$ (P_21/m, ICSD 426247). SEM images for (b) $BiPO_4$-DEG and (c) $BiPO_4$-HT. (d) TEM images for $BiPO_4$-DEG.

Fig. 3 (a) HCHO yield and (b) CH_4 conversion as a function of reaction temperature and (c) selectivity for HCHO as a function of CH_4 conversion over $BiPO_4$-DEG, $FePO_4$, $BiPO_4$-HT, α-Bi_2O_3, and β-Bi_2O_3 catalysts. Reaction conditions: catalyst (100 mg), $CH_4/O_2/N_2$ (2/2/6 sccm), 420–600 °C. (d) Time-on-stream performance of $BiPO_4$-DEG for oxidation of CH_4. Reaction conditions: $BiPO_4$-DEG (100 mg), $CH_4/O_2/N_2$ (2/2/6 sccm), 550 °C.

Carbon balance (%) = (carbon of (CO, CO_2, HCHO) + carbon of output CH_4)/carbon of input $CH_4 \times 100$. In each case, the carbon balance was in the range of 98.7 ± 1.4%.

2.5. Pulse-reaction experiments for CH_4 oxidation

The pulse-reaction experiments were performed using a quartz reactor (4 mm inner diameter at the catalyst bed portion) over a plug of quartz wool. The exit gas was directly connected to a gas chromatograph with a TCD (Shimadzu, GC-8A), and $HCHO/CO_2$ and CO were analyzed using Porapak-N and molecular sieves 5A columns, respectively. The details of the pulse-reactions of He-treated $BiPO_4$-DEG
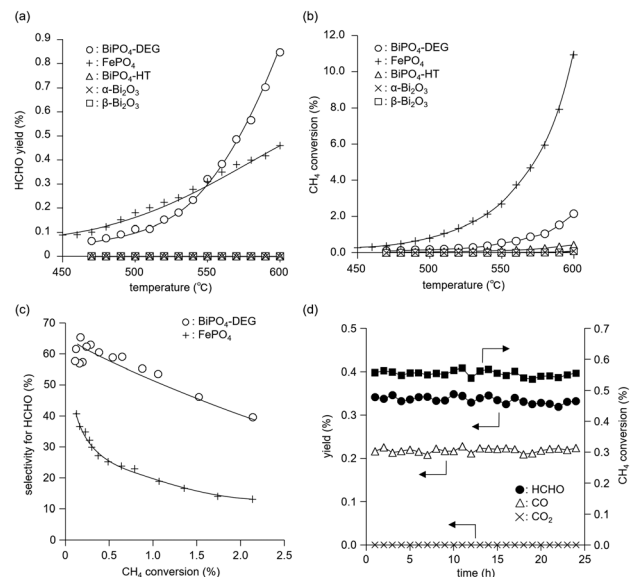
with (i) CH_4 or (ii) CH_4/O_2 pulse are as follows. Prior to the pulse-reaction experiments, $BiPO_4$-DEG (100 mg) was pretreated in a He flow (20 sccm) at 600 °C for 30 min followed by (i) CH_4 pulse (1 mL) or (ii) CH_4/O_2 pulse (1 mL, 1/1 v/v) through the catalyst bed at 600 °C.

2.6. Computational details

The energy evaluation and geometry optimization of the atomic positions were carried out according to the following procedure. The initial atomic positions for the oxides were obtained from the experimental structure of monazite-type monoclinic $BiPO_4$ ($P2_1/n$) taken from the inorganic crystal structure database (ICSD) with ID = 426 231. The unit cell consists of a $2 \times 2 \times 3$ supercell, and the lower 2/3 of the unit cell was fixed during the geometry optimization. The core electrons were represented by the projector augmented-wave (PAW) method,[62] and the valence electrons were expanded by the plane wave basis set up to a cutoff energy of 400 eV. The meta-GGA SCAN functional was used as the exchange–correlation functional in the DFT calculations.[63] The Gaussian smearing method with $\sigma = 0.1$ was used throughout for the smearing of the electron occupation near the Fermi level. The convergence thresholds for the electronic state calculation and geometry optimization were set to 1.0×10^{-5} eV and 0.03 eV Å^{-1} in energy and force, respectively. Integration in the reciprocal lattice space was performed by numerical integration using k-points, which were placed such that the spacing between them was 0.3 Å^{-1}. The gamma point was always included. For isolated molecule calculations (H_2,

5182 | *Catal. Sci. Technol.*, 2023, **13**, 5180–5189

This journal is © The Royal Society of Chemistry 2023

O_2, CH_3, and CH_4), a single k-point was placed on the gamma point. A vacuum layer with a thickness of 12 Å was placed between the slabs, and a dipole correction in the z-direction was introduced to remove the artificial interaction between slabs. All the calculations were performed with the Vienna *ab initio* simulation package (VASP) version 5.4.[64,65]

2.7. *Operando* near ambient pressure X-ray photoelectron spectroscopy (NAP-XPS) experiment

NAP-XPS analysis was performed at the Taiwan Light Source (TLS) beamline 24A of the National Synchrotron Radiation Research Center (NSRRC), Taiwan. The tested sample was pelleted and the spectra were recorded at 550 °C under evacuation and in O_2 atmosphere (0.1 mbar) in the NAP-XPS chamber. P 2p signal at 133.2 eV was used to correct the energy shift.

3. Results and discussion

3.1. Synthesis and characterization of bismuth phosphate nanoparticles

The low solubility of Bi species (*e.g.*, $Bi(NO_3)_3$) in aqueous media typically requires severe reaction conditions such as hydrothermal treatment to obtain bismuth phosphate ($BiPO_4$) catalyst materials, which results in low specific surface areas. Thus, solvothermal and related synthesis methods are more effective for the synthesis of $BiPO_4$ nanoparticles. We also synthesized $BiPO_4$ nanoparticles ($BiPO_4$-DEG) by the calcination of a precursor, which was prepared by the reaction of $Bi(NO_3)_3 \cdot 5H_2O$ and $NH_4H_2PO_4$ in a mixed solution of diethylene glycol (DEG)/water, in air at 600 °C.

The XRD patterns for the precursor and $BiPO_4$-DEG showed the formation of hydrated bismuth phosphate in the trigonal system ($BiPO_4 \cdot (H_2O)_{0.67}$) and a mixture of monoclinic $BiPO_4$ (P_21/n and P_21/m), respectively (Fig. 2(a)). Braque and co-workers reported that the trigonal phase of $BiPO_4 \cdot (H_2O)_{0.67}$ (Fig. 1(a)) is metastable and irreversibly transforms to the monazite-type structure (P_21/n, Fig. 1(b)) and that this monazite-type $BiPO_4$ slowly transforms into the high-temperature monoclinic form (P_21/m, Fig. 1(c)) when heated above 600 °C.[66] No impurity phases such as bismuth phosphates, bismuth oxides, or phosphorous oxides were observed. Elemental analysis of $BiPO_4$-DEG using energy dispersive X-ray fluorescence spectroscopy (ED-XRF) showed that the molar ratio of Bi/P was 1/1, which also supports the high purity. On the other hand, only the monazite-type structure was observed for $BiPO_4$-HT synthesized by the hydrothermal reaction of $Bi(NO_3)_3$ and $(NH_4)_2HPO_4$ at 180 °C followed by calcination at 600 °C in a similar manner to that of previous reports (Fig. S1†).[47,49]

The specific surface area of $BiPO_4$-DEG was 10 m² g⁻¹, which is much larger than that of $BiPO_4$-HT (<1 m² g⁻¹) (Table 1). SEM observations of $BiPO_4$-DEG showed the formation of spherical nanoparticles with estimated particle sizes of *ca.* 50–100 nm (Fig. 2(b)), while large particles with sizes of hundreds of nanometers were observed for $BiPO_4$-HT

Table 1 Specific surface area, bulk content, and particle and crystallite size of the bismuth-based catalysts

Entry	Catalyst	S_{BET} (m² g⁻¹)	Crystallite size[a] (nm)
1	$BiPO_4$-DEG precursor	14	38 (110)
2	$BiPO_4$-DEG	10	P_21/n: 46 (10−1)
			P_21/m: 51 (12−1)
3	$BiPO_4$-HT	<1	93 (10−1)
4	α-Bi_2O_3	1	97 (002)
5	β-Bi_2O_3	10	70 (201)
6[b]	$FePO_4$	22	33 (100)
			22 (200)

[a] Calculated by the XRD peaks using Rigaku PDXL2 software. [b] Data from ref. 44.

(Fig. 2(c)). These nanoparticle sizes were in reasonable agreement with the grain sizes (d = 46 and 51 nm for $BiPO_4$ (P_21/n and P_21/m), respectively) calculated from the (10−1) and (12−1) diffraction lines, respectively, using Scherrer's equation. A similar morphology and size distribution of the nanoparticles were observed by TEM, with clear lattice fringes throughout the particles indicating their crystallinity (Fig. 2(d)). The distances between fringes of different particles were 0.47 and 0.39 nm, assigned to the d-spacing for the (011) planes of monazite-type (P_21/n) and high-temperature monoclinic $BiPO_4$ (P_21/m), respectively.[47,50]

3.2. Catalytic oxidation of CH_4 into HCHO with O_2

The catalyst effect of bismuth-based materials ($BiPO_4$-DEG, $BiPO_4$-HT, α-Bi_2O_3 (Fig. 1(d)), and β-Bi_2O_3 (Fig. 1(e))) was investigated for the oxidation of CH_4 with O_2 as the sole oxidant. There were three main products, *i.e.*, such as formaldehyde (HCHO), carbon monoxide (CO), and carbon dioxide (CO_2). Other products such as CH_3OH were not observed (Fig. S2†). Fig. 3(a) shows the HCHO yield as a function of reaction temperature under a CH_4/O_2/N_2 (2/2/6 sccm) flow in the temperature range of 450–600 °C. $BiPO_4$-DEG selectively gave HCHO with little formation of CO_2. The formation of CO_2 was mainly observed using other bismuth-based catalysts such as $BiPO_4$-HT, α-Bi_2O_3, and β-Bi_2O_3 (Fig. 3(a) and S2†). There was no significant change in the XRD patterns for any of the Bi-based catalysts recovered after CH_4 oxidation (Fig. S3†), although some β-Bi_2O_3 was changed to α-Bi_2O_3, which suggests that the catalytic performance is derived from their structures. Although the water vapor plays an important role in the oxidative conversion of CH_4 in some cases,[67] the presence of water vapor did not enhance the present CH_4 oxidation and HCHO yield/selectivity. The space time yield of $BiPO_4$-DEG at 600 °C was 0.45 mmol$_{HCHO}$ g⁻¹ h⁻¹ (HCHO selectivity: 40%), and the value and selectivity for HCHO were higher than those for previously-reported Bi-based catalysts such as Bi_2O_3–B_2O_3/SiO_2 (4.3 × 10⁻² mmol$_{HCHO}$ g⁻¹ h⁻¹, HCHO selectivity: 30%, 550 °C)[23] and Bi–P–O (7.7 × 10⁻² mmol$_{HCHO}$ g⁻¹ h⁻¹, HCHO selectivity: 4%, 700 °C).[26]

Next, the catalytic performance of $BiPO_4$-DEG was compared with that of $FePO_4$ nanoparticles, which are

effective heterogeneous catalysts for the direct oxidation of CH_4 into HCHO.[44] $BiPO_4$-DEG functioned as a solid catalyst to efficiently give HCHO at high reaction temperatures compared to $FePO_4$ (Fig. 3(a)). The HCHO yield of $BiPO_4$-DEG exceeded that of $FePO_4$ above 550 °C, while $FePO_4$ showed higher HCHO yield than $BiPO_4$-DEG below 550 °C. Notably, a significant difference in the selectivity for HCHO was observed between these two catalysts. Fig. 3(b) and (c) show the dependence of CH_4 conversion on the reaction temperature and the relationship between selectivity to HCHO and CH_4 conversion, respectively. In the case of $FePO_4$, the CH_4 conversion increased up to *ca.* 10% at 600 °C and the selectivity for HCHO was *ca.* 15–40% in the range of ~2% CH_4 conversion. On the other hand, $BiPO_4$-DEG showed *ca.* 40–70% selectivity for HCHO in the same CH_4 conversion region, which suggests that $BiPO_4$-DEG more selectively promotes the direct oxidation of CH_4 into HCHO than $FePO_4$. $BiPO_4$-DEG also exhibited durability without significant change in the selectivity for HCHO (60.6 ± 1.6%) and CO (39.4 ± 1.6%) and CH_4 conversion (0.55 ± 0.02%) at 550 °C for 24 h time-on-stream as shown in Fig. 3(d). On the other hand, the CO yield gradually decreased from 1.29% (1 h) to 0.52% (12 h) for the CH_4 oxidation at 600 °C (Fig. S4(a)†), whereas the HCHO yield was not significantly changed for 12 h and CO_2 was hardly formed in a similar way to the oxidation at 550 °C. Despite such a decrease in the CO yield, the HCHO yield and selectivity after 12 h were 0.74% and 59%, respectively, and higher than those of $FePO_4$ (0.42% yield and 4% selectivity) at 600 °C. From the XRD pattern for the recovered $BiPO_4$-DEG catalyst after the reaction at 600 °C (Fig. S4(b)†), there was a structural change in the grain sizes for $BiPO_4$-DEG calculated from the diffraction lines using Scherrer's equation (from 46 to 82 nm for $P2_1/n$; from 51 to 56 nm for $P2_1/m$) and the ratio of $P2_1/n$ to $P2_1/m$ (from 50/50 to 20/80); thus, the bulk structures of $BiPO_4$ gradually changed during the CH_4 oxidation at 600 °C in sharp contrast to the reaction at 550 °C.

The temperature dependence of CH_4 conversion and product selectivity in CH_4 oxidation with $BiPO_4$-DEG is shown in Fig. 4(a). HCHO was selectively formed in the low-temperature region (~550 °C), and the CH_4 conversion and selectivity for CO gradually increased with increasing reaction temperature. Fig. 4(b) shows the dependence of the CH_4 conversion and selectivity for each product on the contact time (W/F_{CH_4}). HCHO selectivity decreased with increasing W/F_{CH_4} but the CH_4 conversion and CO selectivity increased, which suggests that HCHO is the primary product and CO is formed by sequential oxidation of HCHO. Such over-oxidation of HCHO into CO and CO_2 is also observed in the direct oxidation of CH_4 with $FePO_4$.[44]

3.3. Mechanistic studies on direct oxidation of CH_4 into HCHO over $BiPO_4$

We previously reported that not only the oxidizing ability of metal phosphates but also the surface acid–base properties
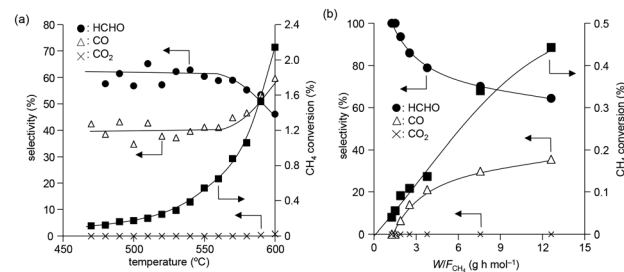

Fig. 4 (a) Product selectivity and CH_4 conversion as function of reaction temperature with O_2 over $BiPO_4$-DEG. Reaction conditions: $BiPO_4$-DEG (100 mg), $CH_4/O_2/N_2$ (2/2/6 sccm). (b) Effect of W/F_{CH_4} on product selectivity and CH_4 conversion. Reaction conditions: $BiPO_4$-DEG (100 mg), $CH_4/O_2/N_2$ (38 : 8 : 54 molar ratio; total 7.8–78 sccm), reaction temperature (550 °C).

are key factors in the direct and selective oxidation of CH_4.[28,43,44] To investigate the oxidizing ability of Bi-based catalysts, H_2-temperature-programmed reduction (H_2-TPR) profiles were measured from 50 to 650 °C (Fig. 5). The reduction of β-Bi_2O_3 started around 250 °C, but the reduction of bismuth phosphates occurred at higher temperatures (from ~350 °C). The H_2 consumption estimated from the H_2-TPR profiles below 550 °C decreased in the order of β-Bi_2O_3 (6.01 mmol g^{-1}) > $BiPO_4$-DEG (3.53 mmol g^{-1}) > α-Bi_2O_3 (3.13 mmol g^{-1}) > $BiPO_4$-HT (1.03 mmol g^{-1}) > $FePO_4$ (0.93 mmol g^{-1}),[44] which is significantly different from the order of CH_4 conversion at 550 °C ($FePO_4$ (2.69%) > $BiPO_4$-DEG (0.54%) > $BiPO_4$-HT (0.12%) > α-Bi_2O_3 (<0.01%) > β-Bi_2O_3 (0%)) (Fig. S5†). In addition, the onset reduction temperature increased in the order of β-Bi_2O_3 (270 °C) < $BiPO_4$-DEG (320 °C) < α-Bi_2O_3 (350 °C) < $FePO_4$ (450 °C) < $BiPO_4$-HT (490 °C), and the order is also inconsistent with the order of reactivity for CH_4 oxidation. A good correlation between H_2 consumption and CH_4 conversion has been reported in the case of iron-based phosphates and oxides.[44] Thus, the
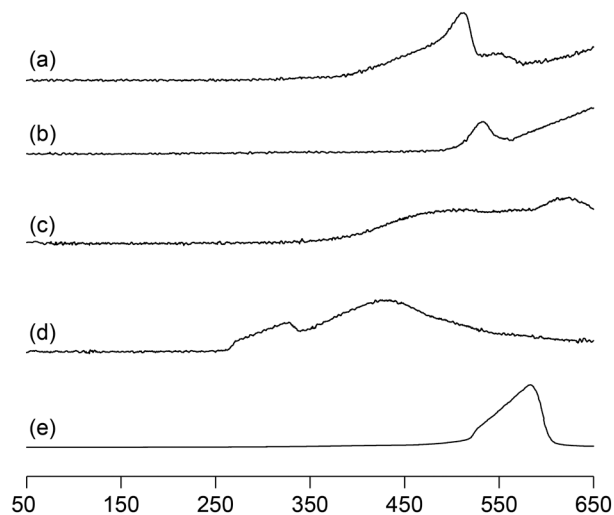

Fig. 5 H_2-TPR profiles for (a) $BiPO_4$-DEG, (b) $BiPO_4$-HT, (c) α-Bi_2O_3, (d) β-Bi_2O_3, and (e) $FePO_4$.

5184 | *Catal. Sci. Technol.*, 2023, **13**, 5180–5189

This journal is © The Royal Society of Chemistry 2023

present discrepancy cannot be explained by the reaction mechanism in which lattice oxygen atoms of metal phosphates and oxides are involved in CH_4 oxidation.

Pulse-reaction experiments for $BiPO_4$-DEG pretreated in He at 600 °C were conducted to determine the origin of the oxygen atoms incorporated in the oxygenated products (*i.e.*, from the oxygen atoms in $BiPO_4$ solid or the surface oxygen species generated from gaseous O_2) (Table 2). No formation of oxygenated products was observed in the reaction of only the CH_4 pulse with $BiPO_4$-DEG in sharp contrast to the $FePO_4$ nanoparticles that reacted with CH_4 to give C_1 products (HCHO and CO_x) and partially reduced $FePO_{4-\delta}$.[44] On the other hand, HCHO, CO, and CO_2 were formed with selectivities of 44%, 54%, and 2%, respectively, at 0.9% CH_4 conversion when the $CH_4 + O_2$ pulse (1/1, v/v) was passed through the catalyst bed at 600 °C. The formation of C_2-coupling products such as ethane and ethylene was not observed for both the pulse reaction and catalytic oxidation of CH_4 over $BiPO_4$-DEG. Oxidative coupling of CH_4 (OCM) typically proceeds under the harsh reaction conditions (>650 °C) to cleave the strong C–H bonds of CH_4, and it is well accepted that the generation of methyl radicals by the solid-catalyst surface with subsequent gas-phase propagation and termination is involved in the OCM mechanism.[2,4,13] These results suggest that the surface oxygen species generated from O_2 and $BiPO_4$ likely reacted with CH_4 to yield C_1 products (HCHO and CO_x) without the formation of methyl radicals in the gas-phase. The kinetics of CH_4 oxidation over $BiPO_4$-DEG at 550 °C were investigated. Fig. 6(a)–(c) show the dependence of the reaction rate (CH_4 conversion) on the partial pressures of CH_4 (P_{CH_4}) and O_2 (P_{O_2}), and the catalyst loading of $BiPO_4$-DEG. A first-order dependence of the reaction rates on P_{CH_4} and catalyst loading was observed (Fig. 6(a) and (c)). The dependence of the reaction rate on P_{O_2} exhibited saturation kinetics (Fig. 6(b)), which is consistent with the Langmuir–Hinshelwood mechanism through adsorption (*i.e.*, activation) of O_2.[68–71]

XPS measurements were performed to further investigate the surface structures of $BiPO_4$-DEG. For the XPS Bi 4f spectrum of $BiPO_4$-DEG at room temperature, a main peak around 159.8 eV (Bi $4f_{7/2}$) assignable to Bi^{3+} species in $BiPO_4$ and a slight peak around 155.9 eV of metallic Bi species were observed (Fig. 7(a)).[72,73] Such formation of metallic Bi species has also been reported for $BiPO_4$ synthesized in ethylene glycol solvent probably due to the weak reducing ability of
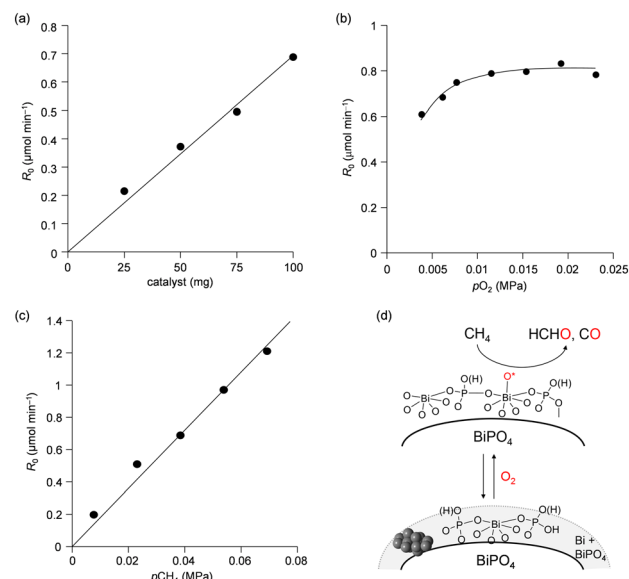

Fig. 6 Effect of (a) catalyst amount and partial pressure of (b) O_2 and (c) CH_4 on reaction rate. Reaction conditions for (a): $BiPO_4$-DEG (25–100 mg), $CH_4/O_2/N_2$ (5/1/7 sccm; total 13 sccm), reaction temperature (550 °C). Reaction conditions for (b): $BiPO_4$-DEG (100 mg), $CH_4/O_2/N_2$ (5/0.5–3/7.5–5 sccm; total 13 sccm), reaction temperature (550 °C). Reaction conditions for (c): $BiPO_4$-DEG (100 mg), $CH_4/O_2/N_2$ (1–9/1/11–3 sccm; total 13 sccm), reaction temperature (550 °C). (d) Proposed reaction mechanism for oxidation of CH_4 with O_2 over $BiPO_4$-DEG.

ethylene glycol.[48] It has also been reported that the formation of surface oxygen vacancies of $BiPO_4$ leads to the disordered edge of $BiPO_4$ particles observed by TEM analyses.[51] In the case of $BiPO_4$-DEG, the edge of the nanoparticles become disordered (thickness ~1 nm, Fig. 2(d)), which supports the formation of metallic Bi species. The XPS O 1s spectrum of
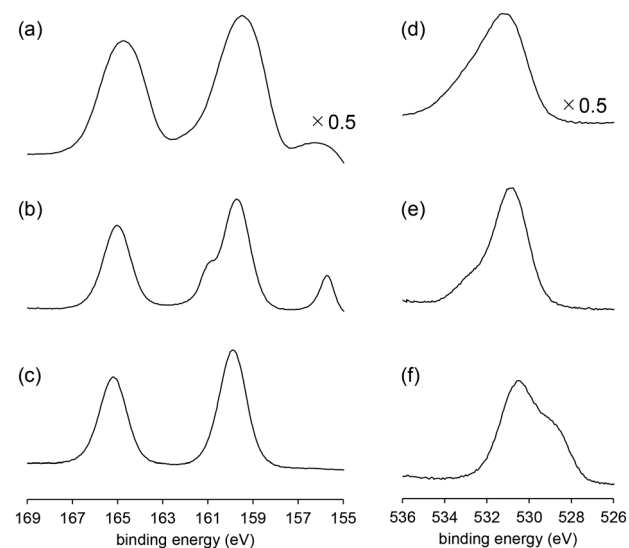
Table 2 Pulse reaction experiments on oxidation of CH_4 with $BiPO_4$-DEG[a]

Entry	Pulse	CH_4 conversion (%)	Yield (%) (selectivity (%))		
			HCHO	CO	CO_2
1	CH_4	<0.01	<0.01 (—)	<0.01 (—)	<0.01 (—)
2	$CH_4 + O_2$ (1/1, v/v)	0.93	0.41 (44)	0.50 (54)	0.02 (2)

[a] Reaction conditions: $BiPO_4$-DEG (100 mg), He (20 sccm), pulse volume (1 mL), reaction temperature (600 °C).

Fig. 7 XPS (a–c) Bi 4f and (d–f) O 1s spectra of $BiPO_4$-DEG. (a and d) $BiPO_4$-DEG at room temperature under evacuation, (b and e) $BiPO_4$-DEG at 550 °C under evacuation, and (c and f) $BiPO_4$-DEG at 550 °C under O_2 (0.1 mbar).

This journal is © The Royal Society of Chemistry 2023

Catal. Sci. Technol., 2023, **13**, 5180–5189 | **5185**

BiPO$_4$-DEG also showed a peak around 533 eV which corresponds to adsorbed water in addition to the main peak around 531 eV assignable to lattice oxygen of BiPO$_4$.

Surface oxygen species are formed on a CePO$_4$ catalyst through the activation of the O$_2$ molecule assisted by the electric field. Such active oxygen species possibly facilitate the oxidative coupling of the CH$_4$ reaction even at low temperature. In this case, the surface Lewis acidic Ce sites would play an important role in the activation of O$_2$.[28,43] Therefore, the surface acid properties of the present BiPO$_4$-DEG catalyst were investigated by IR measurements of samples adsorbed with pyridine and acetone. The IR spectrum for pyridine-adsorbed BiPO$_4$-DEG showed a band at 1446 cm^{-1} assignable to the pyridine species coordinated to the Lewis acid sites, and no band at 1540 cm^{-1} due to pyridinium ions bonded to the Brønsted acid sites (Fig. 8(a)). The amount of Lewis acid sites was estimated to be 26 µmol g^{-1} from the intensity of the band at 1446 cm^{-1}. The density of surface Bi cations on BiPO$_4$-DEG was calculated to be 1.6 nm^{-2} from the BET surface area of BiPO$_4$-DEG and the amounts of Lewis acid sites measured using pyridine-adsorbed IR. This value was comparable to that for monoclinic CePO$_4$ nanorods (1.6 nm^{-2}) with monazite-type structure and the calculated value estimated from the main surface structure obtained from HAADF-STEM observation.[28,29] The IR spectrum of acetone adsorbed on BiPO$_4$-DEG (Fig. 8(b)) showed one strong C=O stretching band due to acetone molecules coordinated to Lewis acid sites, with the band position at a lower wavenumber (1683 cm^{-1}) than those for acetone in the gas phase (1731 cm^{-1}), CePO$_4$ (1699 cm^{-1}), and FePO$_4$ (1685 cm^{-1}).[28,43,44] All these results support the presence of uniform surface Lewis acidic Bi species on the BiPO$_4$-DEG nanoparticles. Such coordinatively unsaturated sites would be involved in the O$_2$ activation. In addition, the basicity was also evaluated by IR spectroscopy with adsorbed CHCl$_3$ and CH$_3$OH (Fig. 8(c) and (d)). The presence of weakly-basic phosphate units on BiPO$_4$ was confirmed,‡ which likely contributes to

the suppression of complete oxidation to CO$_2$ in a similar way to the CH$_4$ oxidation over FePO$_4$.[44]

To obtain information on possible active oxygen species formed on surface Bi sites, an *operando* near-ambient-pressure X-ray photoelectron spectroscopy (NAP-XPS) experiment was conducted under O$_2$ atmosphere. When BiPO$_4$-DEG was exposed to O$_2$ (0.1 mbar) at 550 °C, only the peak corresponding to BiPO$_4$ was observed in the XPS Bi 4f spectra with the disappearance of the peak of metallic Bi, which suggests reconstruction of the surface structure. The XPS O 1s spectra also changed during the reaction of BiPO$_4$-DEG with O$_2$. While the main peak around 531 eV assignable to lattice oxygens of BiPO$_4$ was unchanged, the peak around 533 eV corresponding to adsorbed oxygen atoms disappeared and a new peak around 529 eV appeared upon exposure of O$_2$. It has been reported that the peaks due to bismuth oxides are in the range of 528.8–529.9 eV and that the negative shift of O 1s peaks is likely caused by the presence of non-bridging Bi–O species.[74–78] Thus, the new peak may be caused by surface oxygen species such as Bi–O species generated on BiPO$_4$, which possibly react with CH$_4$ to give HCHO as a primary product. There was no significant difference in the XPS Bi 4f spectra between the fresh and recovered BiPO$_4$-DEG catalysts after the CH$_4$ oxidation under the conditions in Fig. S6,† which suggests that the *in situ* generated oxygen species observed in the reaction temperature range play an important role in the present CH$_4$ oxidation.

To further investigate possible involvement of surface active oxygen species on BiPO$_4$, density functional theory (DFT) calculations were carried out. Since the surface Bi density of BiPO$_4$-DEG was comparable to that of monoclinic CePO$_4$ nanorods as described above, the monazite-type structure ($P_2$1/n) was used as a model catalyst for the CH$_4$ oxidation. Surface energy calculations for the (100), (110), and (111) surfaces of BiPO$_4$ identified that the (100) surface is the most stable one. Furthermore, the DFT-based thermodynamic analysis have shown that the partially oxidized BiPO$_4$ (100) surface (0.25 monolayer) in which O atom adsorbed on Bi is the stable surface under the reaction environment (see the details in ESI,† Fig. S7 and S8). The following two pathways the CH$_4$ activation were compared: (i) H-abstraction by surface O atom and CH$_3$ adsorption on PO$_4$ units, and (ii) H-abstraction by lattice O atom and CH$_3$ adsorption on PO$_4$ units. Fig. 9 shows the optimized geometry and the reaction energies for CH$_4$ activation by these two pathways. The reaction energy (ΔE) is
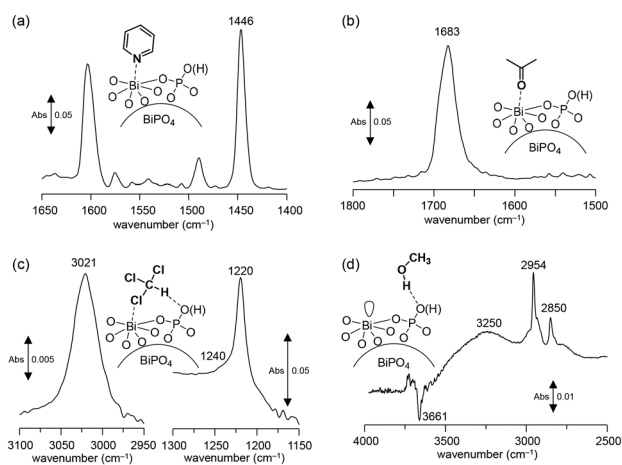

Fig. 8 Difference IR spectra for (a) pyridine-, (b) acetone-, (c) chloroform-, and (d) CH$_3$OH-adsorbed BiPO$_4$-DEG at 25 °C.

‡ The basicity was confirmed by IR spectroscopy with adsorbed CHCl$_3$ (Fig. 8(c) and (d)). The red-shift of the original C–H stretching mode of the CHCl$_3$ molecule from 3034 cm^{-1} to 3021 cm^{-1} indicates the presence of basic sites on the surface.[74] The band shift (13 cm^{-1}) was larger than that for FePO$_4$ (~1 cm^{-1}) but lower than that for CePO$_4$ (26 cm^{-1}); thus, the basicity of BiPO$_4$ was stronger than that of FePO$_4$ but weaker than that of CePO$_4$.[39,40] In the IR spectrum of BiPO$_4$-DEG with adsorbed CH$_3$OH, broad bands between 3000 and 3500 cm^{-1} appeared with negative v(O–H) bands, and bands at 2954 and 2850 cm^{-1} assignable to the asymmetric and symmetric CH$_3$ stretching modes of molecularly adsorbed CH$_3$OH, respectively, were observed. All these results are consistent with previous reports for the interaction of probe molecules on metal phosphates with uniform Lewis acid sites and weak base sites.
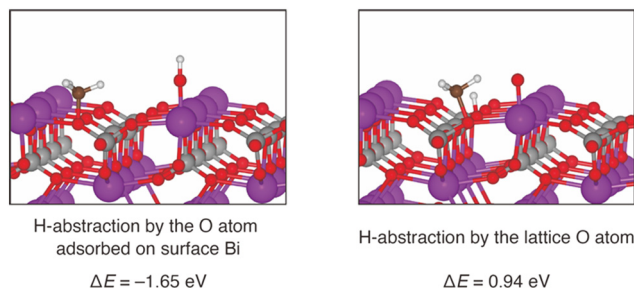
5186 | *Catal. Sci. Technol.*, 2023, **13**, 5180–5189

This journal is © The Royal Society of Chemistry 2023

Fig. 9 Optimized structure of the product state of the CH_4 activation on 0.25 ML Bi-oxidized $BiPO_4$ (100) surface. Two reaction pathways are considered, and their reaction energies (ΔEs) calculated with the DFT are shown.

defined as the dissociative adsorption energy of CH_4. H-abstraction using a surface O atom is an exothermic reaction, since the calculated ΔE is -1.65 eV. On the other hand, H-abstraction by a lattice O atom is an endothermic reaction ($\Delta E = 0.94$ eV). Thus, our calculations indicate that the CH_4 activation takes place using surface O atoms, and not lattice O atoms. The surface O atoms are formed from gaseous O_2 in the inlet gas, and therefore CH_4 activation requires the presence of O_2. This is consistent with the observed reaction rate dependence on P_{O_2} as seen in Fig. 6. In addition to the possible involvement of surface oxygen species generated on $BiPO_4$, the weak basicity on $BiPO_4$ (Fig. 8(c) and (d)),‡ similar to those on $FePO_4$ and $CePO_4$, likely leads to high HCHO selectivity of $BiPO_4$-DEG.[79]

Conclusions

In summary, bismuth-based phosphate and oxide catalysts were investigated for the oxidation of CH_4 with O_2 as the sole oxidant. Monoclinic $BiPO_4$ nanoparticles ($BiPO_4$-DEG) exhibited higher catalytic performance for the direct oxidation of CH_4 into HCHO than $BiPO_4$ synthesized by the hydrothermal method ($BiPO_4$-HT), α-Bi_2O_3, and β-Bi_2O_3. The lack of correlation between the catalytic activity and oxidizing ability estimated by H_2-TPR and pulse reaction experiments suggested that CH_4 oxidation did not proceed with lattice oxygen supplied from the $BiPO_4$-DEG solid. On the basis of mechanistic studies including the catalyst effect, kinetics, NAP-XPS, and DFT calculations, the oxidation of CH_4 may proceed at surface oxygen species generated on surface Bi atoms of $BiPO_4$. IR spectroscopy measurements of $BiPO_4$-DEG with adsorbed probe molecules indicate the presence of uniform Lewis acid sites and weak basic sites, which possibly activate O_2 and suppress subsequent oxidation into CO_2, respectively. Such a possible O_2 activation mode for $BiPO_4$-DEG would result in high selective formation of HCHO at high temperatures in sharp contrast to $FePO_4$ nanoparticles with the redox mechanism.

Author contributions

A. M. and K. O. designed the experiments, performed the experimental investigation, and conducted data analyses with the help of K. K. A. I. performed the DFT calculations. M. T., C. W., Y. L. performed the NAP-XPS analyses. K. K., A. I., and Y. L. wrote the paper. The draft was reviewed by A. M., A. I., Y. L., M. H. and K. K.

Conflicts of interest

There are no conflicts to declare.

Acknowledgements

Notes and references

1 D. Saha, H. A. Grappe, A. Chakraborty and G. Orkoulas, *Chem. Rev.*, 2016, **116**, 11436–11499.
2 R. Horn and R. Schlögl, *Catal. Lett.*, 2015, **145**, 23–39.
3 A. Abdulrasheed, A. A. Jalil, Y. Gambo, M. Ibrahim, H. U. Hambali and M. Y. Shahul Hamid, *Renewable Sustainable Energy Rev.*, 2019, **108**, 175–193.
4 C. Hammond, S. Conrad and I. Hermans, *ChemSusChem*, 2012, **5**, 1668–1686.
5 K. Otsuka and Y. Wang, *Appl. Catal., A*, 2001, **222**, 145–161.
6 A. I. Olivos-Suarez, À. Szécsényi, E. J. M. Hensen, J. Ruiz-Martinez, E. A. Pidko and J. Gascon, *ACS Catal.*, 2016, **6**, 2965–2981.
7 M. Ravi, M. Ranocchiari and J. A. van Bokhoven, *Angew. Chem., Int. Ed.*, 2017, **56**, 16464–16483.
8 A. V. Vekki and S. T. Marakaev, *Russ. J. Appl. Chem.*, 2009, **82**, 521–536.
9 A. H. Bagherzadeh Mostaghimi, T. A. Al-Attas, M. G. Kibria and S. Siahrostami, *J. Mater. Chem. A*, 2020, **8**, 15575–15590.
10 S. Ogo and Y. Sekine, *Chem. Rec.*, 2017, **17**, 726–738.
11 I. Vollmer, I. Yarulina, F. Kapteijn and J. Gascon, *ChemCatChem*, 2018, **11**, 39–52.
12 K. Sun, D. M. Ginosar, T. He, Y. Zhang, M. Fan and R. Chen, *Ind. Eng. Chem. Res.*, 2018, **57**, 1768–1789.
13 H. Schwarz, *Angew. Chem., Int. Ed.*, 2011, **50**, 10096–10115.
14 M. H. Mahyuddin, Y. Shiota and K. Yoshizawa, *Catal. Sci. Technol.*, 2019, **9**, 1744–1768.
15 Z. Jin, L. Wang, E. Zuidema, K. Mondal, M. Zhang, J. Zhang, C. Wang, X. Meng, H. Yang, C. Mesters and F.-S. Xiao, *Science*, 2020, **367**, 193–197.
16 P. Xiao, Y. Wang, T. Nishitoba, J. N. Kondo and T. Yokoi, *Chem. Commun.*, 2019, **55**, 2896–2899.
17 C. Hammond, M. M. Forde, M. H. Ab Rahim, A. Thetford, Q. He, R. L. Jenkins, N. Dimitratos, J. A. Lopez-Sanchez, N. F. Dummer, D. M. Murphy, A. F. Carley, S. H. Taylor, D. J.

This journal is © The Royal Society of Chemistry 2023

Catal. Sci. Technol., 2023, **13**, 5180–5189 | **5187**

Willock, E. E. Stangland, J. Kang, H. Hagen, C. J. Kiely and G. J. Hutchings, *Angew. Chem., Int. Ed.*, 2012, **51**, 5129–5133.

18 B. E. R. Snyder, M. L. Bols, R. A. Schoonheydt, B. F. Sels and E. I. Solomon, *Chem. Rev.*, 2018, **118**, 2718–2768.

19 P. Schwach, M. G. Willinger, A. Trunschke and R. Schlögl, *Angew. Chem., Int. Ed.*, 2013, **52**, 11381–11384.

20 J. H. Lunsford, *Angew. Chem., Int. Ed. Engl.*, 1995, **34**, 970–980.

21 B. P. C. Hereijgers and B. M. Weckhuysen, *ChemSusChem*, 2009, **2**, 743–748.

22 M. Bugnola, R. Carmieli and R. Neumann, *ACS Catal.*, 2018, **8**, 3232–3236.

23 K. Otsuka and M. Hatano, *J. Catal.*, 1987, **108**, 252–255.

24 K. Harrath, X. Yu, H. Xiao and J. Li, *ACS Catal.*, 2019, **9**, 8903–8909.

25 C. Williams, J. H. Carter, N. F. Dummer, Y. K. Chow, D. J. Morgan, S. Yacob, P. Serna, D. J. Willock, R. J. Meyer, S. H. Taylor and G. J. Hutchings, *ACS Catal.*, 2018, **8**, 2567–2576.

26 T. Ohno and J. B. Moffat, *Catal. Lett.*, 1992, **16**, 181–190.

27 A. V. Annapragada and E. Gulari, *J. Catal.*, 1990, **123**, 130–146.

28 A. Sato, S. Ogo, K. Kamata, Y. Takeno, T. Yabe, T. Yamamoto, S. Matsumura, M. Hara and Y. Sekine, *Chem. Commun.*, 2019, **55**, 4019–4022.

29 V. Paunović, G. Zichittella, M. Moser, A. P. Amrute and J. Pérez-Ramirez, *Nat. Chem.*, 2016, **8**, 803–809.

30 G. Zichittella, V. Paunović, A. P. Amrute and J. Pérez-Ramírez, *ACS Catal.*, 2017, **7**, 1805–1817.

31 Y. Wang and K. Otsuka, *J. Catal.*, 1995, **155**, 256–267.

32 Y. Wang, X. Wang, Z. Su, Q. Guo, Q. Tang, Q. Zhang and H. Wan, *Catal. Today*, 2004, **93–95**, 155–161.

33 G. O. Alptekin, A. M. Herring, D. L. Williamson, T. R. Ohno and R. L. McCormick, *J. Catal.*, 1999, **181**, 104–112.

34 Y. Wang and K. Otsuka, *J. Mol. Catal. A: Chem.*, 1996, **111**, 341–356.

35 Y. Wang and K. Otsuka, *J. Chem. Soc., Faraday Trans.*, 1995, **91**, 3953–3961.

36 V. Gomonaj and H. Toulhoat, *ACS Catal.*, 2018, **8**, 8263–8272.

37 J. Baek, B. Rungtaweevoranit, X. Pei, M. Park, S. C. Fakra, Y.-S. Liu, R. Matheu, S. A. Alshmimri, S. Alshehri, C. A. Trickett, G. A. Somorjai and O. M. Yaghi, *J. Am. Chem. Soc.*, 2018, **140**, 18208–18216.

38 T. Ikuno, J. Zheng, A. Vjunov, M. Sanchez-Sanchez, M. A. Ortuno, D. R. Pahls, J. L. Fulton, D. M. Camaioni, Z. Li, D. Ray, B. L. Mehdi, N. D. Browning, O. K. Farha, J. T. Hupp, C. J. Cramer, L. Gagliardi and J. A. Lercher, *J. Am. Chem. Soc.*, 2017, **139**, 10294–10301.

39 V. Fornés, C. López, H. H. López and A. Martínez, *Appl. Catal., A*, 2003, **249**, 345–354.

40 H. Launay, S. Loridant, A. Pigamo, J. L. Dubois and J. M. M. Millet, *J. Catal.*, 2007, **246**, 390–398.

41 T. Akiyama, R. Sei and S. Takenaka, *Catal. Sci. Technol.*, 2021, **11**, 5273–5281.

42 J. Tian, J. Tan, Z. Zhang, P. Han, M. Yin, S. Wan, J. Lin, S. Wang and Y. Wang, *Nat. Commun.*, 2020, **11**, 5693.

43 S. Kanai, I. Nagahara, Y. Kita, K. Kamata and M. Hara, *Chem. Sci.*, 2017, **8**, 3146–3153.

44 A. Matsuda, H. Tateno, K. Kamata and M. Hara, *Catal. Sci. Technol.*, 2021, **11**, 6987–6998.

45 P. Sprenger, W. Kleist and J.-D. Grunwaldt, *ACS Catal.*, 2017, **7**, 5628–5642.

46 W. K. Darkwah, B. B. Adormaa, M. K. C. Sandrine and Y. Ao, *Catal. Sci. Technol.*, 2019, **9**, 546–566.

47 C. Pan, J. Xu, Y. Chen and Y. Zhu, *Appl. Catal., B*, 2012, **115–116**, 314–319.

48 F. Tian, H. Zhao, G. Li, Z. Dai, Y. Liu and R. Chen, *ChemSusChem*, 2016, **9**, 1579–1585.

49 J. Xu, L. Li, C. Guo, Y. Zhang and W. Meng, *Appl. Catal., B*, 2013, **130–131**, 285–292.

50 Y. Guo, P. Wang, J. Qian, Y. Ao, C. Wang and J. Hou, *Appl. Catal., B*, 2018, **234**, 90–99.

51 Y. Lv, Y. Zhu and Y. Zhu, *J. Phys. Chem. C*, 2013, **117**, 18520–18528.

52 F. Qiu, L. T. Weng, P. Ruiz and B. Delmon, *Appl. Catal.*, 1989, **47**, 115–123.

53 N. Abadzhjieva, P. Tzokov, I. Uzunov, V. Minkov, D. Klissurski and V. Rives, *React. Kinet. Catal. Lett.*, 1994, **53**, 413–418.

54 M. Ruwet, S. Ceckiewicz and B. Delmon, *Ind. Eng. Chem. Res.*, 1987, **26**, 1981–1983.

55 T.-S. Chang, L. Guijia, C.-H. Shin, Y. K. Lee and S.-S. Yun, *Catal. Lett.*, 2000, **68**, 229–234.

56 Y. Takita, M. Ninomiya, R. Matsuzaki, H. Wakamatsu, H. Nishiguchi and T. Ishihara, *Phys. Chem. Chem. Phys.*, 1999, **1**, 2367–2372.

57 B. Gallace and J. B. Moffat, *J. Catal.*, 1982, **76**, 182.

58 F. Pazoki, S. Bagheri, M. Shamsayei, M. J. Nejad and A. Heydari, *Mater. Chem. Phys.*, 2020, **253**, 123327.

59 T. Aihara, W. Aoki, S. Kiyohara, Y. Kumagai, K. Kamata and M. Hara, *ACS Appl. Mater. Interfaces*, 2023, **15**, 17957–17968.

60 M. Koutani, E. Hayashi, K. Kamata and M. Hara, *J. Am. Chem. Soc.*, 2022, **144**, 14090–14100.

61 Y. Yamaguchi, R. Aono, E. Hayashi, K. Kamata and M. Hara, *ACS Appl. Mater. Interfaces*, 2020, **12**, 36004–36013.

62 P. E. Blochl, *Phys. Rev. B: Condens. Matter Mater. Phys.*, 1994, **50**, 17953–17979.

63 J. Sun, A. Ruzsinszky and J. P. Perdew, *Phys. Rev. Lett.*, 2015, **115**, 036402.

64 G. Kresse and J. Furthmuller, *Phys. Rev. B: Condens. Matter Mater. Phys.*, 1996, **54**, 11169–11186.

65 G. Kresse and J. Furthmuller, *Comput. Mater. Sci.*, 1996, **6**, 15–50.

66 B. Romero, S. Bruque, M. A. G. Aranda and J. E. Iglesias, *Inorg. Chem.*, 2002, **33**, 1869–1874.

67 K. Takanabe and E. Iglesia, *Angew. Chem., Int. Ed.*, 2008, **47**, 7689–7693.

68 E. Hayashi, T. Tamura, T. Aihara, K. Kamata and M. Hara, *ACS Appl. Mater. Interfaces*, 2022, **14**, 6528–6537.

69 K. Sugahara, K. Kamata, S. Muratsugu and M. Hara, *ACS Omega*, 2017, **2**, 1608–1616.

70 S. Kawasaki, K. Kamata and M. Hara, *ChemCatChem*, 2016, **8**, 3247–3253.

71 V. D. Makwana, Y. C. Son, A. R. Howell and S. L. Suib, *J. Catal.*, 2002, **210**, 46–52.

72 P. Deng, H. Wang, R. Qi, J. Zhu, S. Chen, F. Yang, L. Zhou, K. Qi, H. Liu and B. Y. Xia, *ACS Catal.*, 2020, **10**, 743–750.

73 Q. Jing, L. Huang, Q. Li, Y. Song and L. Chen, *J. Mater. Sci.: Mater. Electron.*, 2020, **31**, 20954–20963.

74 J. Gong, C. S. Lee, E. J. Kim, J. H. Kim, W. Lee and Y. S. Chang, *ACS Appl. Mater. Interfaces*, 2017, **9**, 28426–28432.

75 J. Liu, S. Guo, H. Wu, X. Zhang, J. Li and K. Zhou, *J. Mater. Sci. Technol.*, 2021, **85**, 1–10.

76 J. Sun, J. Wen, G. Wu, Z. Zhang, X. Chen, G. Wang and M. Liu, *Adv. Funct. Mater.*, 2020, **30**, 2004108.

77 Q. Chen, Y. Wang and H. Wang, *J. Non-Cryst. Solids*, 2018, **481**, 85–93.

78 L. N. Elliott, D. Austin, R. A. Bourne, A. Hassanpour, J. Robb, J. L. Edwards, S. Sutcliffe and T. N. Hunter, *Langmuir*, 2023, **39**, 5697–5709.

79 T. Komanoya, K. Nakajima, M. Kitano and M. Hara, *J. Phys. Chem. C*, 2015, **119**, 26540–26546.

This journal is © The Royal Society of Chemistry 2023

Catal. Sci. Technol., 2023, **13**, 5180–5189 | **5189**